Available online at www.sciencedirect.com

ScienceDirect

Nuclear Physics A 921 (2014) 60–84

NUCLEAR PHYSICS A

www.elsevier.com/locate/nuclphysa

Emission of forward neutrons by 158A GeV indium nuclei in collisions with Al, Cu, Sn and Pb

E.V. Karpechev [a], I.A. Pshenichnov [a,*], T.L. Karavicheva [a], A.B. Kurepin [a], M.B. Golubeva [a], F.F. Guber [a], A.I. Maevskaya [a], A.I. Reshetin [a], V.V. Tiflov [a,1], N.S. Topilskaya [a], P. Cortese [b], G. Dellacasa [b,1], R. Arnaldi [c], N. De Marco [c], A. Ferretti [c], M. Gallio [c], A. Musso [c], C. Oppedisano [c], A. Piccotti [c,1], E. Scomparin [c], E. Vercellin [c], C. Cicalò [d], G. Puddu [d], E. Siddi [d], P. Szymanski [e,f], I. Efthymiopoulos [e]

[a] *Institute for Nuclear Research, Russian Academy of Sciences, 117312 Moscow, Russia*
[b] *Dipartimento di Scienze e Tecnologie Avanzate and INFN, Corso Borsalino 54, 15100 Alessandria, Italy*
[c] *Università di Torino and INFN, Via Pietro Giuria 1, 10125 Torino, Italy*
[d] *Università di Cagliari and INFN, Casella Postale 170, 09042 Monserrato (Cagliari), Italy*
[e] *CERN, EP Division, CH-1211, Geneva 23, Switzerland*
[f] *Soltan Institute for Nuclear Studies, Warsaw, Poland*

Received 3 August 2013; received in revised form 30 October 2013; accepted 12 November 2013

Available online 14 November 2013

Abstract

The cross sections of forward emission of one, two and three neutrons by 158A GeV ^{115}In nuclei in collisions with Al, Cu, Sn and Pb targets are reported. The measurements were performed in the framework of the ALICE–LUMI experiment at the SPS facility at CERN. Various corrections accounting for the absorption of beam nuclei and produced neutrons in target material and surrounding air were introduced. The corrected cross section data are compared with the predictions of the RELDIS model for electromagnetic fragmentation of ^{115}In in ultraperipheral collisions, as well as with the results of the abrasion–ablation model for neutron emission in hadronic interactions. The measured neutron emission cross sections well agree with the RELDIS results, with the exception of In–Al collisions where the measured cross sections are larger compared to RELDIS. This is attributed to a relatively large contribution of hadronic fragmentation

* Corresponding author.
E-mail address: pshenich@inr.ru (I.A. Pshenichnov).
[1] Deceased.

http://dx.doi.org/10.1016/j.nuclphysa.2013.11.003

of In on Al target with respect to electromagnetic fragmentation, in contrast to similar measurements performed earlier with 30A GeV ^{208}Pb colliding with Al.

Keywords: Electromagnetic dissociation of nuclei; Ultraperipheral nucleus–nucleus collisions; Zero degree calorimeters

1. Introduction

The researches studying nucleus–nucleus collisions at the Super Proton Synchrotron (SPS) and at the Large Hadron Collider (LHC) at CERN are mostly focused on the studies of hot and dense nuclear matter, which is created in collisions of ultrarelativistic nuclei. This includes the search of signals of the phase transition between the hadronic matter and the quark–gluon phase which can be produced in collisions with small impact parameters. Such central collisions are characterized by a large overlap of the volumes of colliding nuclei, their complete disintegration and very high multiplicities of produced secondary particles.

The studies of collisions of ultrarelativistic nuclei remain incomplete without exploring the domain of large impact parameters. There is another phenomenon which deserves attention there, namely, ultraperipheral interactions of nuclei which occur without any overlap of their volumes. The disintegration of nuclei in collisions with impact parameters $b \geqslant R_1 + R_2$, where R_1 and R_2 are the nuclear radii, can only be explained by the long-range electromagnetic forces.

The impact of the Coulomb field of a fast-moving nucleus with the charge Z on its collision partner can be estimated as following. Providing that in the rest frame of the collision partner the moving nucleus has the Lorentz factor γ, the Lorentz-boosted Coulomb potential at the moment of the closest approach can be estimated as $V_c = \alpha\gamma Z/b$, where α is the fine structure constant. Therefore, for collisions of medium-weight nuclei ($Z \sim 50$, $b \sim 10$ fm) with beam energies available at the CERN SPS the relation $\alpha\gamma \sim 1$ holds and $V_c \sim 1$ GeV. The estimated V_c essentially exceeds the effective nuclear potential ~ 50 MeV, which confines nucleons inside nuclei. This explains the emission of single nucleons from nuclei and their fragmentation as a result of electromagnetic interactions in ultraperipheral collisions. This phenomenon is well-known as electromagnetic dissociation (EMD) of nuclei [1–3]. The behavior of nuclear matter under the impact of strong electromagnetic fields can be studied in ultraperipheral collisions of ultrarelativistic nuclei.

The Lorentz contraction of electromagnetic fields of nuclei in ultraperipheral nucleus–nucleus collisions at the LHC becomes tremendous. As demonstrated by recent measurements [4,5], the total cross section of neutron emission from at least one of the colliding lead nuclei approaches 187 b at 1.38A TeV + 1.38A TeV collision energy. In this case the nucleus which impacts another nucleus via the action of its electromagnetic field is characterized by a large Lorentz factor $\gamma \sim 4.3 \times 10^6$ which defines the scale of contraction.

As demonstrated in several publications, the EMD process plays a certain role at the LHC. On the one hand a large EMD cross section imposes restrictions on the beam lifetime at the LHC [6]. Nuclear fragments produced in EMD events can lead to local heating of the LHC construction elements [7,8]. On the other hand, the collider luminosity can be monitored [9] by counting mutual EMD events characterized by the simultaneous emission of forward neutrons by each of the nuclei in a single ultraperipheral event. As suggested [3,10], the rate R_m^{EMD} of mutual EMD events with the emission of either one or two neutrons in the directions of each beam should be measured

at the LHC. This makes possible to measure the collider luminosity $L = R_m^{EMD}/\sigma_m^{EMD}$ providing that the mutual EMD cross section σ_m^{EMD} is calculated with sufficient accuracy [3,10,11].

The single and mutual EMD neutron emission cross sections can be calculated with the RELDIS Monte Carlo model [10–13], which is based on the Weizäcker–Williams method [1]. In order to ensure the accuracy of this model for Pb–Pb collisions at the LHC, its results were validated at lower collision energies. In particular, we have measured the cross sections of forward neutron emission from 30A GeV lead nuclei in collisions with various target nuclei [14]. As proved by these measurements [14], the cross sections of forward emission of one and two neutrons are well described by the RELDIS model. Recently the single and mutual EMD cross sections of neutron emission were measured at the LHC for Pb–Pb collisions at 1.38A TeV + 1.38A TeV [4,5], and a very good agreement with the RELDIS results was demonstrated.

In the future the research programs at the CERN-SPS and LHC can be extended to study collisions of medium-weight nuclei. It is the purpose of the present work to study the electromagnetic dissociation of indium nuclei in ultrarelativistic collisions with aluminum, copper, tin and lead target nuclei. The cross sections of forward emission of one, two and three neutrons by 158A GeV ^{115}In nuclei are measured and compared to the corresponding results of the RELDIS model. The fragmentation of 158A GeV indium nuclei in collisions with Si, Ge, Sn, W and Pb was studied in Ref. [15] by measuring the cross sections of production of secondary fragments with specific charge, also known as the charge-changing cross sections. Since neither fragment masses, nor neutrons emitted from indium nuclei were identified in Ref. [15], the measured cross sections represented the sum of hadronic fragmentation cross sections due to direct overlap of nuclei and fragmentation cross sections in ultraperipheral collisions. In contrast to Ref. [15], mainly the contribution of electromagnetic dissociation was identified in our experiment due to the detection of forward neutrons from indium nuclei, as explained below. In this sense our data complement the data collected in Ref. [15] and provide specific information on electromagnetic interactions of ultrarelativistic ^{115}In nuclei.

2. Neutron emission from indium nuclei in collisions with target nuclei

We consider now the neutron emission from indium nuclei resulting from electromagnetic and hadronic interactions of these nuclei with various targets. Once theoretical models describing such processes are at hand, the relations between the cross sections of such processes can be estimated along with energy and angular distributions of produced neutrons. This helps in estimating the parameters of our experimental setup which is designed to detect such neutrons.

2.1. Neutrons from electromagnetic dissociation of indium nuclei

The Weizsäcker–Williams method of virtual photons [1–3] is widely used to describe ultraperipheral interactions of nuclei. According to this method electromagnetic interactions of nuclei proceed by emission and absorption of virtual photons by these nuclei. The range of equivalent photon energies from the nucleon emission threshold E_{min} to $E_{max} \sim \gamma/(R_1 + R_2)$ [11] should be taken into account in order to describe the electromagnetic dissociation of nuclei. According to the threshold of (γ, n) reaction on ^{115}In, $E_{min} = 9.26$ MeV was adopted in our calculations. The maximum photon energy E_{max} depends on the sizes of colliding nuclei: $E_{max} = 3.32$ and 2.36 GeV for ultraperipheral interactions of 158A GeV ^{115}In with Al and Pb nuclei, respectively. The equivalent photon spectrum calculated with various assumptions is given in Refs. [1–3].

The RELDIS model uses the Monte Carlo method to simulate EMD events. This model is described in Refs. [10–13]. The absorption and emission of one and two photons in a single ultraperipheral collision is taken into account, and the hadronic production of secondary particles in each collision is simulated by the Monte Carlo method. Depending on the energy E of a photon which is absorbed by a nucleus, various processes take place, namely, the excitation of a giant resonance in this nucleus, the absorption of the photon by a pair of bound nucleons or the production of hadrons on a bound nucleon.

It is expected that the excitation and decay of the giant dipole resonance (GDR) at $9 \leqslant E \leqslant 35$ MeV provides the main contribution to electromagnetic dissociation of indium nuclei. Therefore, below we briefly review the modeling of the GDR excitation and decay within the RELDIS model. This process usually leads to the emission of one or two neutrons from In nucleus. The fission of In is not probable, and the cross section of emission of protons following the absorption of low-energy photons is also small due to a high Coulomb barrier in this medium-weight nucleus. The total probability of photon absorption is calculated as an integral of the product of the equivalent photon spectrum and the total photoabsorption cross section [10,11].

It is assumed that the energy of a photon of $9 \leqslant E \leqslant 35$ MeV is completely transformed into the excitation energy of the nucleus which absorbs this photon. The subsequent evolution of an excited nucleus is described by the Statistical Multifragmentation Model (SMM) [16], which is widely used to describe decays of excited nuclear systems. As predicted by the RELDIS model, the mean excitation energy of a medium-weight or heavy excited system, e.g., In or Pb, after the absorption of a photon is below 2 MeV/nucleon [10,11]. The SMM model predicts that the de-excitation of such systems proceeds via a sequential evaporation of nucleons. In particular, there is a competition between the emission of one and two neutrons in the GDR energy region, see Fig. 1. As only neutrons were detected in experiments carried out in several laboratories [17–19], (γ, n) and $(\gamma, 2n)$ channels were not separated from (γ, np) and $(\gamma, 2np)$, respectively. Therefore, their sum is presented in Fig. 1 at $E \leqslant 35$ MeV and will be referred below as (γ, n) and $(\gamma, 2n)$, respectively, in order to simplify notations.

The most reliable evaluated nuclear data on (γ, n) and $(\gamma, 2n)$ cross sections on ^{115}In were obtained in Ref. [20] based both on theoretical results and measurements. The total photoabsorption cross section was estimated from measurements [17–19], while the pre-equilibrium model of photonuclear reactions was used to disentangle the contributions of (γ, n) and $(\gamma, 2n)$ processes.

In the RELDIS model the total photoabsorption cross section in the Giant Resonance region ($E \leqslant 40$ MeV) is calculated according to the approximations found in Refs. [22,23] for various medium-weight and heavy target nuclei, including In. The relations between (γ, n) and $(\gamma, 2n)$ channels are calculated by RELDIS from the statistical evaporation model. As seen from Fig. 1, the experimental data on (γ, n) reaction on In collected at the Livermore National Laboratory [18] are described by RELDIS in general. However, the threshold of $(\gamma, 2n)$ reaction is overestimated. Nevertheless, the RELDIS results on $(\gamma, 2n)$ reaction remain closer to Livermore data [18] compared to other measurements [17,19]. At the same time on the right-hand side of the GDR resonance the RELDIS results on (γ, n) reaction are higher compared to the corresponding evaluated cross section data [20]. An opposite trend is seen for the evaluated $(\gamma, 2n)$ [20] cross section. It is higher compared to the same cross section calculated by RELDIS.

Neutrons emitted by excited ultrarelativistic nuclei created in ultraperipheral collisions have very forward angular distributions in the lab frame. This is because such neutrons have few MeV kinetic energy and they are evaporated isotropically in the rest frame of the excited nucleus. After the Lorentz boost from this system to the laboratory system such neutrons have velocities close to the velocity of the beam nuclei and they are characterized by small transverse momenta P_t

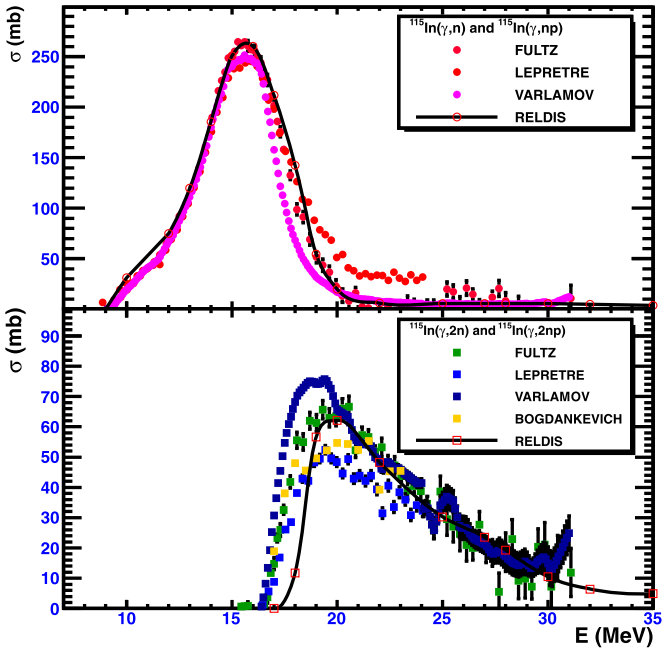

Fig. 1. Cross sections of emission of one (top panel) and two neutrons (bottom panel) by ^{115}In as a result of absorption of a photon with energy E. Experimental data [17–19] and evaluated data [20] all extracted from the EXFOR database [21] are shown by various symbols explained on the legends of the corresponding panels. Results of the RELDIS code are shown by open symbols connected by a solid line.

perpendicular to the beam direction. Distributions of P_t for first and second neutrons emitted in electromagnetic dissociation of lead nuclei were calculated with RELDIS [14]. They have a maximum at $P_t \sim 0.02$–0.04 GeV/c and a tail extending up to $P_t \sim 0.15$ GeV/c [14]. Similar distributions, also restricted by $P_t < 0.15$ GeV/c, are calculated with RELDIS for 158A GeV ^{115}In nuclei. They indicate that all EMD neutrons are emitted within ± 1 mrad angle with respect to the beam direction. The location of the neutron calorimeter (1350 cm downstream from the target) and its transverse extensions (~ 3.5 cm at each direction perpendicular to the beam axis) ensure the detection of all neutrons produced in EMD of 158A GeV ^{115}In nuclei, as a wider angle of ± 2.6 mrad is covered by the detector.

2.2. *Neutron emission in nuclear reactions induced by indium nuclei*

Hadronic interactions of nuclei are characterized by strong interactions between participating nucleons in the overlapping parts of colliding nuclei. The abrasion–ablation model provides a simplified description of such collisions, and its modern version was already used to describe the fragmentation of lead nuclei [24] with the same (158 GeV) beam energy per nucleon as of indium beam in the present work.

Following the abrasion–ablation model nucleons from colliding nuclei are classified into participants and spectators according to their role in the collision [24]. Participant nucleons interact with nucleons from collision partner. Spectator nucleons represent relatively cold spectator nuclear matter and do not interact with nucleons of collision partner at the first abrasion stage of the collision. The number of participant nucleons is calculated according to the Glauber theory

of multiple scattering. Other details of the abrasion–ablation model used in the present work are given elsewhere [24].

In Ref. [24] various methods to calculate the excitation energy of residual nuclei composed of spectator nucleons were presented. Hereafter such nuclei are called prefragments. As shown [24], the excitation energy of a prefragment can be estimated as 13–26 MeV on average per each participant nucleon knocked out from the initial nucleus. Excited prefragments decay at the ablation stage of the collision and their decays in most cases are simulated as evaporation of nucleons according to the above-mentioned statistical model SMM [16].

Neutrons are produced on both stages of interaction, but their kinematic characteristics are different. Nucleons are knocked out from initial nuclei as a result of individual nucleon–nucleon collisions at the abrasion stage, and their emission is accompanied by production of secondary hadrons. The average transverse momentum of nucleons knocked out from nuclei is estimated as $\langle P_t \rangle \sim 0.2$–$0.4$ GeV/c [24], and it is essentially larger than the average transverse momentum of neutrons produced in electromagnetic dissociation of nuclei. However, neutrons emitted by excited prefragments at the ablation stage have a narrow P_t-distribution, similar to the distribution of neutrons from electromagnetic dissociation. Such ablation neutrons can be also registered by the calorimeter used in the present work.

Hadronic nucleus–nucleus collisions lead to emission of various numbers of neutrons in each event. As expected, the average number of knocked out and emitted neutrons per event depends on the collision centrality, i.e. on the impact parameter b. Since the fragmentation events of indium nuclei which specifically lead to the emission of one, two and three neutrons is the main subject of our study, peripheral (grazing) nucleus–nucleus collisions with $b \sim R_1 + R_2$ have to be considered. The number of participant nucleons in such peripheral collisions is small and such nucleons are mostly located in a thin surface layer of each nucleus. This explains the fact that the cross section of emission of a small number of nucleons amounts to a small fraction of the total fragmentation cross section. In addition to the direct knock-out of nucleons at the abrasion stage the evaporation of nucleons from excited residual nuclei takes place also at the ablation stage. In this case the events with emission of only few neutrons at the ablation stage are mostly classified as peripheral collisions characterized by relatively low excitation of spectator matter.

Despite of the simplifications adopted in the above-described modeling of nucleus–nucleus collisions, a satisfactory agreement of calculated and measured yields of nuclear fragments can be expected. As shown in Ref. [24], this approach applied to peripheral collisions of 158A GeV lead nuclei with C, Al, Cu, Sn and Au successfully describes the yields of nuclear fragments which are close in mass and charge to projectile nuclei. Such fragments are created after emitting a few nucleons, and the nucleon multiplicity in such reactions is accordingly described. Therefore, one can expect that the abrasion–ablation model is also applicable to neutron emission by indium projectiles with the same beam energy per nucleon.

Calculated cross sections of emission of one, two and three neutrons, possibly accompanied by other undetected particles, e.g. protons, are collected in Table 1. The total EMD and hadronic fragmentation cross sections are also given in this table. Due to the presence of channels with emission of more than three neutrons in electromagnetic and hadronic interactions, the sum of 1nX, 2nX and 3nX cross sections is less than the corresponding total cross section. The sum of 1nX, 2nX and 3nX EMD channels amounts to 87% of the total EMD cross section, while the same channels of hadronic fragmentation provide only 6–8% of the total hadronic cross section.

Table 1
Calculated cross sections of emission of one, two and three neutrons and the total cross sections for electromagnetic dissociation and hadronic fragmentation of 158A GeV ^{115}In on Al, Cu, Sn and Pb nuclei. Results of the RELDIS and abrasion–ablation models are given for electromagnetic and hadronic interactions of nuclei.

Target nucleus	Fragmentation channel	EMD, RELDIS (barns)	Hadronic fragmentation, abrasion–ablation (barns)
Al	1nX	0.40	0.06
	2nX	0.09	0.08
	3nX	0.03	0.11
	total	0.60	3.34
Cu	1nX	1.91	0.07
	2nX	0.45	0.10
	3nX	0.13	0.12
	total	2.86	4.25
Sn	1nX	5.47	0.08
	2nX	1.28	0.11
	3nX	0.38	0.13
	total	8.19	5.14
Pb	1nX	14.05	0.09
	2nX	3.32	0.12
	3nX	1.03	0.15
	total	21.07	6.18

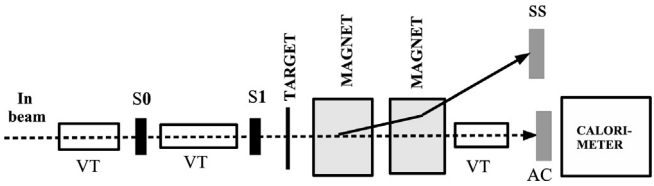

Fig. 2. Experimental setup to study neutron emission in electromagnetic fragmentation of 158A GeV ^{115}In. S0, S1, SS, AC – scintillator detectors, VT – vacuum tubes.

3. Experimental setup

Measurements of the cross sections of emission of forward neutrons in fragmentation of 158A GeV indium nuclei were performed at H8 beam line of the CERN-SPS accelerator with a setup shown in Fig. 2. The beam of ^{115}In nuclei of 158A GeV energy was focused on a target which can be moved into and out of the beam by means of a mobile support.

Two plastic scintillator detectors, S0 and S1, were installed in front of the target. Both detectors were made of polystyrene with addition of 4–5% of PTP POPOP. They were manufactured as thin plates each 2 mm thick and of 2 cm × 2 cm size. Both detectors have demonstrated a very good energy resolution. The main peak from 158A GeV indium nuclei was clearly distinguished in the signals taken from both detectors. There were additional tails related to a lower energy deposition in the scintillator plates due to nuclear fragments produced in beam fragmentation. A small tail was also identified in the signal obtained from the S0 detector due to the presence of nuclear fragments created in interactions of beam nuclei with air and windows of vacuum

Table 2
Atomic number Z, atomic mass A, material density ρ and thickness d of the targets used in measurements with 158A GeV ^{115}In beam.

	Al	Cu	Sn	Pb thin	Pb thick
ρ (g/cm^3)	2.7	8.96	7.31	11.35	11.35
d (cm)	1.4	0.45	0.34	0.135	0.294
Z	13	29	50	82	82
A	27	64	119	208	208

tubes on their way to S0. Production of secondary particles in the beam line upstream of the S0 detector also contributed to this tail.

Charged particles were deflected beyond the acceptance of the neutron calorimeter by means of two magnets of 4.4 T × m each. These magnets were placed after the target and they deflected particles in the horizontal direction. Since noninteracting beam nuclei were deflected by 7 cm from the primary beam direction, it was possible to place there a plastic scintillator SS for their detection, as well as for the detection of ^{114}In, ^{113}In and ^{112}In created in EMD. These nuclei were deflected by the magnets by angles which were very close to the deflection angle of the primary beam. Since the SS detector had small dimensions of 2 cm × 2 cm thus covering a small range of defection angles, a certain selectivity of SS to indium remnants created in EMD was achieved. Most of nuclear fragments created in hadronic fragmentation of ^{114}In are expected to have charge-to-mass ratios which differ from the corresponding ratio of beam nuclei and therefore do not hit the SS detector.

Neutrons from fragmentation of In nuclei were not deflected by magnets and therefore hit the neutron calorimeter which was installed after the magnets directly on the axis of the primary beam. The neutron calorimeter was placed on a platform with their surface aligned parallel to the beam axis. An additional detector AC was installed downstream of the target in front of the neutron calorimeter. AC was built as a scintillator detector, it was 2 mm thick with the transverse dimensions of 70 mm × 100 mm. As AC was fired by charged particles, it was used as a veto detector to suppress the events in neutron calorimeter which were due to such particles. The number of primary indium nuclei was defined by counts collected from the S1 detector, while the SS detector was used to tag indium nuclei which did not fragment neither in air, nor in the target.

Four targets made of different materials (aluminum, cooper, tin and lead) were used. In addition the fifth lead target was also used, but with increased thickness. It had the thickness about twice as large as the first lead target. The corrections for the absorption of produced neutrons and multiple interactions of indium nuclei in target material depend on the target thickness. However, providing that such corrections are properly introduced, the cross sections of In–Pb interactions which are calculated from the data collected with thin and thick targets are expected to be equal. A possible difference of resulting cross sections can be considered as a systematic uncertainty of our measurements. The parameters of the targets used in our experiment are listed in Table 2.

During a separate empty-target run only neutrons produced in the beam line collimators, scintillator plates S0 and S1, and also in air were detected by the neutron calorimeter. This provided us the estimation of the neutron background due to nuclear reactions which take place beyond the target. Then this background was subtracted from the signal obtained in other runs with installed targets.

There were several advancements of the described experimental setup with respect to our previous study [14] of fragmentation of 30A GeV lead nuclei in ultraperipheral collisions with same target nuclei. Namely, the following improvements were achieved:

- Vacuum tubes (VT) were placed before and after the S0 detector and also between the magnets and neutron calorimeter. This helped us to reduce, respectively, the numbers of beam nuclei and produced neutrons lost in their interactions with air.
- The AC detector was installed in front of the neutron calorimeter and was used as a veto detector.
- Almost all neutrons from electromagnetic fragmentation of beam nuclei were covered by the acceptance of neutron calorimeter. There was no need in introducing any corrections for a limited acceptance in contrast to our previous measurements, see Ref. [14].

4. Response of the neutron calorimeter to pion and proton beams

The neutron Zero Degree Calorimeter (ZDC) was a key part of the experimental setup designed for the ALICE–LUMI experiment. Its performance was crucial for accurate measurements of neutron yields. Therefore, before the main experiment with indium beam ZDC was tested with beams of other particles of comparable energy. The response functions of the neutron calorimeter to pions and protons are presented in Figs. 3, 4, 5, 6 and 7. The following design requirements are essential for effective registration of neutrons and reliable determination of their multiplicity in each event:

- The response of neutron calorimeter remains constant over the transverse section of this detector with its spot size covering the whole range of transverse momenta of neutrons produced in EMD of beam nuclei. The detector response and relative energy resolution as a function of the transverse shift y of the beam with respect to the central axis of the calorimeter are presented for 100 and 30 GeV pions, in Figs. 3 and 4, respectively.
- The response of the neutron calorimeter is proportional to the projectile energy. This makes possible to disentangle peaks corresponding to one, two and three neutrons. The response of the calorimeter to pions as a function of pion energy is shown in Fig. 5.
- The energy resolution of the calorimeter for neutrons emitted in the EMD process of beam nuclei is sufficient for separation of events with different numbers of neutrons. This is proved by measurements with pion beam. As shown in Fig. 6, the energy resolution improves with the increase of pion energy. As follows from the extrapolation of data shown in Fig. 6 to 158 GeV neutrons from EMD, the relative energy resolution for this case will be better than 20%.

The design of the neutron calorimeter was based on results of Monte Carlo simulations. The calorimeter was assembled as a periodic structure consisting of 40 layers. Each layer was made of three tungsten plates. Each tungsten plate was 2.5 mm thick and paved with a 2 mm thick plastic scintillator plate, all of 7 cm $\times$ 10 cm dimensions. As each layer was tilted by 45 degrees with respect to the beam axis in the vertical direction, the transverse cross section of the calorimeter was 7×7.07 cm^2. The collected light from all scintillator plates was re-emitted into 80 plastic fibers of 1 mm in diameter each glued into the semicircular groves made on the sides of each scintillator plate. These fibers transported light through a fiber bundle to an XP2020

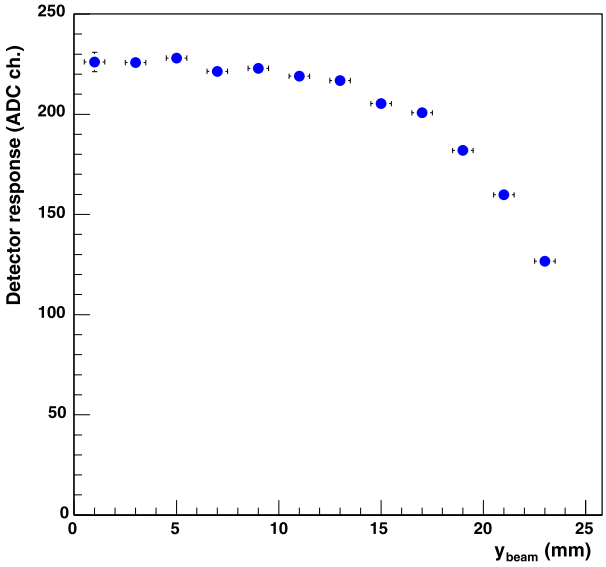

Fig. 3. Response of the calorimeter to 100 GeV pions as a function of transverse shift of the beam axis y with respect to the calorimeter axis.

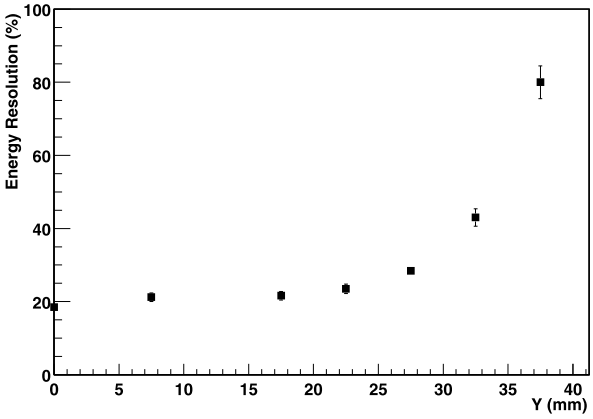

Fig. 4. Relative energy resolution of the calorimeter to 30 GeV pions as a function of transverse shift y with respect to the calorimeter axis.

photomultiplier. The opposite ends of the optical fibers were covered by aluminum film in order to reduce the loss of light.

The X5 beam channel of the CERN SPS was used to calibrate the calorimeter by irradiating it by pions with energy from 10 to 100 GeV and by 30 GeV protons. Two compact scintillator counters of 2 mm $\times$ 2 mm size were used to identify the position of the beam on the forward surface of the calorimeter. The distribution of signal collected from the calorimeter was approximated by a Gaussian function with the amplitude, peak position and width defined by fitting this distribution.

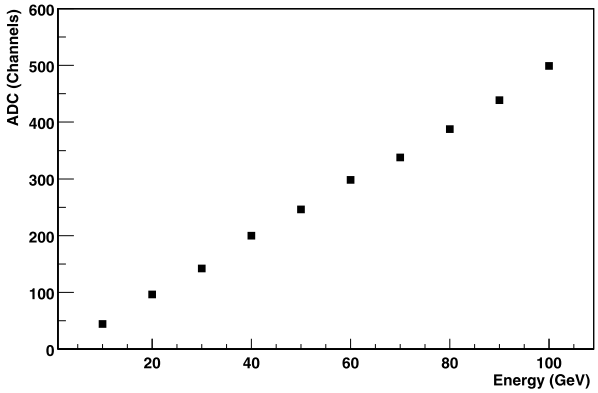

Fig. 5. Response of the calorimeter as a function of pion energy.

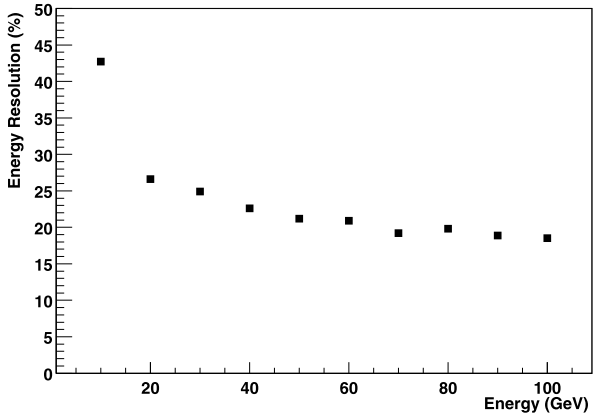

Fig. 6. Relative energy resolution of the calorimeter as a function of pion energy.

As shown in Fig. 5, the response of the calorimeter to pions with energy from 10 to 100 GeV is proportional to pion energy. The relative energy resolution σ/μ of $\sim 25\%$ for 30 GeV protons, Fig. 7, was measured in a dedicated run which provided the energy calibration for the calorimeter. During this run the magnets were switched off.

During another run with a 100 GeV pion beam the response of the calorimeter was measured depending on the beam shift along the horizontal and vertical directions.

5. Measurements with ^{115}In and data processing

The main set of measurements of fragmentation of ^{115}In was performed with a medium-intensity beam of 5×10^5 ions per spill. Three different triggers were used in measurements: (1) a random coincidence trigger to estimate pedestal and noise; (2) a beam trigger only with S0; and (3) a physics trigger for measurements of ^{115}In fragmentation. The main trigger included signals from S0, S1 and SS (S0 $\times$ S1 $\times$ SS) under the condition that the energy registered by the neutron calorimeter exceeds 8 GeV. In addition, some measurements were performed with S0 $\times$ SS trigger. The data collected in such measurements were not used for the determination of

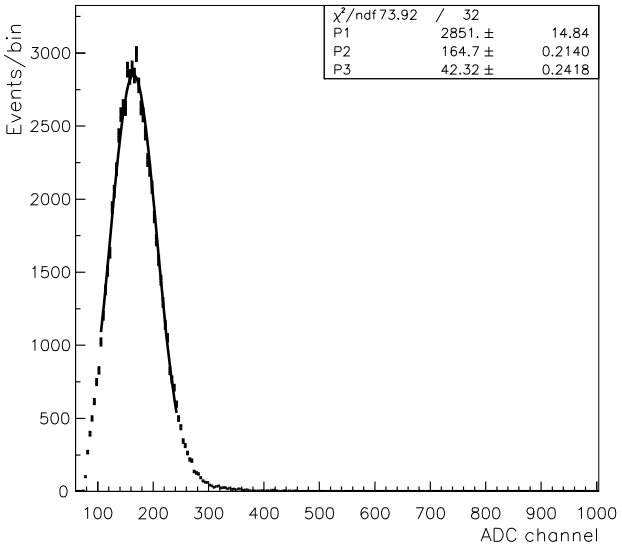

Fig. 7. Energy spectrum of the calorimeter for 30 GeV protons.

the neutron emission cross sections, but rather were used to estimate the corrections to raw data applied in processing data off-line.

The threshold settings of the S0, S1 and SS counters were estimated in runs without target. In these runs the main signal in each of these detectors was due to beam nuclei and the thresholds were adjusted accordingly to avoid the rejection of beam particles and provide similar counting rates. Then the same settings were applied to the S0, S1 and SS counters during runs with target.

During each run the output from the neutron calorimeter was recorded into a separate file containing up to 10^6 events. Each run had its own pedestal run to ascertain an accurate pedestal subtraction. The pedestal corrected data from all runs with a given target were combined into a single data set, after the ADC counts were converted into energies. Each set was used afterwards to estimate neutron emission cross sections for the corresponding target.

It is expected that noninteracting beam nuclei and those which lost only few neutrons after EMD produce similar Gaussian-shape spectra in the S0 and SS detectors. Therefore, the parts of the spectra deviating from this Gaussian function can be attributed to the hadronic interactions of indium nuclei with the target, with air or with the windows of the vacuum tubes. Indeed, the energy per nucleon of secondary nuclear fragments created in hadronic interaction can be quite different from the beam energy, in contrast to the energy of residual nuclei created in the EMD process. The latter process does not change essentially the velocity of a residual nucleus created after the emission of few neutrons from ^{115}In. Therefore, the removal of non-Gaussian contributions from the signals taken from S0 and SS together with the detection of one, two or three neutrons in the calorimeter helps to extract signals from EMD. The fraction of events removed by such a procedure was from 2 to 3.7% for various sets of events.

Several measurements were performed without target. The signal in the neutron calorimeter collected without target, but in coincidence with signals taken from S0 and SS was considered as a background attributed to the interactions of beam nuclei with air, the walls of the vacuum tubes and other components of the setup. It was subtracted from the spectra collected in measurements with target in order to obtain spectra corresponding only to the interactions of beam nuclei with

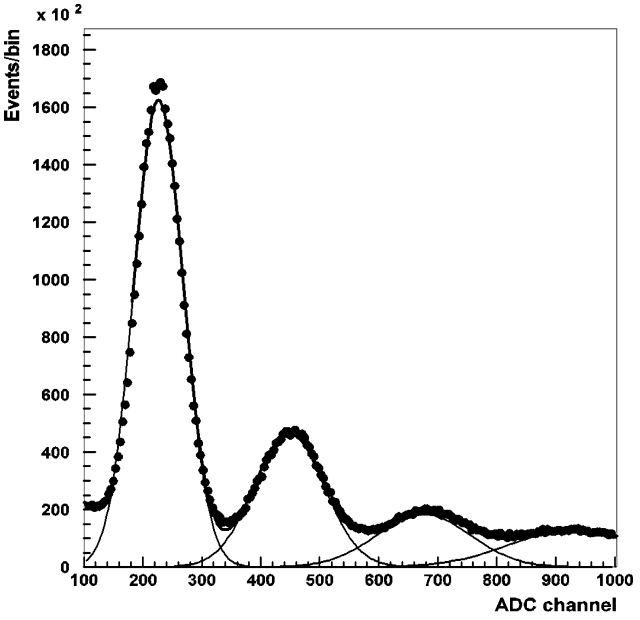

Fig. 8. Energy spectrum of the calorimeter for forward neutrons produced in fragmentation of 158A GeV ^{115}In nuclei.

the target. About 3.7–3.8% of events were removed by this background subtraction. Since the spectra obtained in separate runs with and without target corresponded to different numbers of projectile nuclei, these spectra were appropriately weighted before the subtraction. Namely, the spectrum obtained without target was multiplied by the ratio between the number of beam particles which crossed the target and number of projectile nuclei in the run without target. This ratio was calculated as 0.4–0.8, and the events leading to overflow in the last ADC channels were discarded. The number of events with overflow collected with all five targets was from 4.8% to 6.8%, while it was 4% in the run without target.

One of the resulting spectra obtained with ^{115}In beam is shown in Fig. 8. Three distinct peaks corresponding to one, two and three neutrons which hit the calorimeter in a single event are clearly seen. There is also a less prominent contribution from four and more neutrons. The resulting spectra for each target were fit by a sum of Gaussians. The average value μ_{1n} and dispersion σ_{1n} for the $1n$-peak were introduced as free parameters of the fit. The average values for $2n$, $3n$ and $4n$ events μ_{2n}, μ_{3n} and μ_{4n}, and the corresponding dispersion values σ_{2n}, σ_{3n} and σ_{4n} were calculated through the values for $1n$-peak: $\mu_{2n} = 2\mu_{1n}$, $\sigma_{2n} = \sqrt{2}\sigma_{1n}$, $\mu_{3n} = 3\mu_{1n}$, $\sigma_{3n} = \sqrt{3}\sigma_{1n}$, $\mu_{4n} = 4\mu_{1n}$, $\sigma_{4n} = 2\sigma_{1n}$. The amplitudes of all peaks were the free parameters of the fit.

As found from the analysis of the resulting spectra, the contribution of the $3n$-peak remains essential for estimating $1n$ and $2n$ yields. In particular, the magnitude of the $2n$-peak cannot be accurately estimated without accounting for the $3n$-peak, as there is a large overlap between these peaks and the corresponding Gaussians. The influence of the $4n$-peak on the $3n$-peak is even more important as their widths are larger and they essentially overlap. As seen from Fig. 8, the $4n$-peak cannot be reliably identified, but its presence is essential for extracting the $3n$ yield. In this work quantitative estimates are given for $1n$, $2n$ and $3n$ yields, but a small admixture of four neutrons was also taken into account when fitting the full spectra.

The CERNLIB library was used in fitting the spectra. The area under each peak was calculated by using respective CERNLIB functions and it was assumed proportional to the number of events of each kind ($1n$, $2n$ or $3n$). The absolute number N of events with a given number of neutrons (1, 2 or 3) produced in EMD depends on the target thickness d and the mean free pass length λ with respect to EMD:

$$N = N_0\left(1 - \mathrm{e}^{-d/\lambda}\right). \tag{1}$$

The number of projectile nuclei is denoted here as N_0, $\lambda = 1/n\sigma$ with n defined as the density of nuclei in the target material and σ as the corresponding ($1n$, $2n$ and $3n$) EMD cross sections.

The number of projectiles N_0 was counted by S0. The cross sections extracted from (1) are listed in Table 3. Several corrections which take into account the absorption of beam nuclei due to hadronic fragmentation and secondary nuclear reactions induced by emitted neutrons will be applied to these values in the following sections.

6. Corrections for secondary interactions of neutrons, secondary EMD and hadronic fragmentation of indium nuclei

Neutrons emitted inside the target as a result of EMD can be lost in subsequent interactions with target material and air before they reach the neutron calorimeter. Indeed, neutrons traverse 13 m before they reach the calorimeter and a fraction of them interact with nuclei of gases from which air is composed. The loss of neutrons in the windows of the vacuum tubes can be neglected, as such windows are very thin.

A projectile ^{115}In nucleus can initiate a second EMD event following the emission of one or two neutrons in a first EMD event. Therefore, secondary and even tertiary EMD processes are possible inside the target. Since two subsequent emissions, each of a single neutron, are identified by the calorimeter as a two-neutron event, the yields of $1n$ events will be artificially underestimated in favor of $2n$ events.

During the propagation of beam ^{115}In nuclei and produced neutrons through the target and air a certain sequence of phenomena which affect the measured neutron yields takes place. According to this sequence several corrections are applied to the raw data given in Table 3:

1. Corrections for neutrons lost in nuclear reactions with air.
2. Corrections for neutrons lost in secondary nuclear reactions with target nuclei. The neutrons are either stopped in the target or scattered by a large angle beyond the acceptance of the neutron calorimeter. Due to such losses a real $2n$-event is seen as a $1n$-event, and a $3n$-event as a $2n$- or $1n$-event, respectively. This is because of the absorption or scattering of some neutrons in multi-neutron events.
3. Corrections for secondary EMD. Two subsequent $1n$-emissions from In projectile are detected as a single $2n$-event.
4. Corrections for hadronic fragmentation of ^{115}In in the target. This process competes with EMD and frequently leads to production of multiple nuclear fragments without emission of forward neutrons which have the velocity close to the primary beam velocity.

Since the corrections are applicable to the measured numbers of $1n$, $2n$ and $3n$ events, they will be introduced in the next sections following the above-listed sequence.

Table 3
Uncorrected EMD cross sections. Statistical uncertainties these values are negligible.

Target	Channel	Cross section (barns)
Al	$1n$	0.395
	$2n$	0.167
	$3n$	0.067
Cu	$1n$	1.541
	$2n$	0.515
	$3n$	0.189
Sn	$1n$	4.090
	$2n$	1.300
	$3n$	0.471
Pb thin	$1n$	9.779
	$2n$	3.050
	$3n$	0.953
Pb thick	$1n$	9.750
	$2n$	3.327
	$3n$	1.150

6.1. Corrections for neutron loss in air

The loss of neutrons in air has to be estimated first. The mean free path of ~ 158 GeV neutrons before they interact with air is estimated as:

$$\lambda_{air} = A/(N_A \times \rho_{air} \times \sigma_{nN}). \tag{2}$$

In the following it is taken for simplicity that the average atomic number of air $A = 14$, which corresponds to nitrogen, and its density $\rho_{air} = 0.001205$ g/cm^3. In Eq. (2) the Avogadro's number $N_A = 6.022 \times 10^{23}$ mol^{-1} and the total cross section for neutron interaction with nitrogen $\sigma_{nN} = 380$ mb $= 0.38 \times 10^{-24}$ cm^2 are used. The value of σ_{nN} was calculated for nucleon projectiles by means of the abrasion model based on the Glauber collision theory which was successfully applied to nucleus–nucleus collisions in Ref. [24].

In the case of elastic neutron scattering on a nucleus in air it is very probable that the scattered neutron will not hit the calorimeter. Therefore it is appropriate to use the total cross section in calculating neutron loss in air. The cross section σ_{nN} includes the elastic scattering cross section. The value of σ_{nN} can be also estimated by interpolating experimental data compiled in Ref. [25].

Since the total cross section σ_{nN} for nitrogen target is not reported in the literature for 158 GeV neutrons, other combinations of the target nucleus and neutron energy were used in these estimations. In particular, according to the compilation [25], the total cross section for 52.7 GeV neutrons colliding with ^{16}O amounts to 421 ± 21 mb [26] and 475 ± 44 mb [27] for 1 GeV neutrons, while the total inelastic cross section for the interaction of 100 GeV neutrons with air ($^{15}_{7.2}$Air) is 237 mb [28]. Since a weak energy dependence of the total cross section is expected at high neutron energies, the average of these three measurements was calculated as $\sigma_{nN} = 378$ mb. This value agrees well with $\sigma_{nN} = 380$ mb calculated by the Glauber theory, Ref. [24], as explained above.

Since neutrons traverse the distance of $X = 6.145$ m in air before they reach the neutron calorimeter, $\lambda_{air} \approx 509$ m according to Eq. (2) and the probability W_{nN} to pass this distance without interaction is calculated as:

$$W_{nN} = \mathrm{e}^{-X/\lambda_{air}} = 0.988. \tag{3}$$

The probability of the event with two neutrons escaped from the target and reached the calorimeter without interacting in air is calculated as $W_{2n} = W_{nN}^2 \approx 0.976$, while for all three produced neutrons reached the calorimeter: $W_{3n} = W_{nN}^3 \approx 0.964$.

The probability of such an event when a pair of produced neutrons leave the target without interaction, but then one neutron interacts with air and another one reaches the calorimeter is calculated as:

$$W_{1+} = 2W_{nN}(1 - W_{nN}) \approx 0.024. \tag{4}$$

Due to the loss of one of two neutrons such $2n$ event will be detected as a $1n$ event.

The probability of the event with two of three neutrons interacting with air and with one hitting the calorimeter is given by:

$$W_{1++} = 3W_{nN}(1 - W_{nN})^2 \approx 0.0004. \tag{5}$$

Such a $3n$ event is seen as a $1n$ event.

The probability of the event with one of three neutrons scattered in air and two others reached the calorimeter is calculated as:

$$W_{2+} = 3W_{nN}^2(1 - W_{nN}) \approx 0.035. \tag{6}$$

Such a $3n$ event is seen as a $2n$ event.

The numbers of $1n$, $2n$ and $3n$ events detected by the calorimeter and denoted as $N_{1n\text{-}calo}$, $N_{2n\text{-}calo}$, $N_{3n\text{-}calo}$ are estimated according to the area calculated under each of the Gaussian peaks in the calorimeter energy spectrum, Fig. 8. In the following the numbers of $1n$, $2n$ and $3n$ events immediately after neutron escape from the target, i.e. before neutron propagation through air, are denoted as $N_{1n\text{-}air}$, $N_{2n\text{-}air}$ and $N_{3n\text{-}air}$, respectively.

It is straightforward to apply the correction for neutron absorption in air to the number of registered $3n$ events: $N_{3n\text{-}air} = N_{3n\text{-}calo}/W_{3n}$. In this calculation it is assumed that the number of $4n$ events which are seen as $3n$ events due to the loss of one neutron is negligible.

The number of detected neutron pairs $N_{2n\text{-}calo}$ is composed first from the number of $2n$ events corrected for neutron absorption, and second from the pairs of neutrons reached the calorimeter following the loss of one neutron in $3n$ events:

$$N_{2n\text{-}calo} = N_{2n\text{-}air}W_{2n} + N_{3n\text{-}air}W_{2+}. \tag{7}$$

Therefore, the number of $2n$ events at the moment of neutron escape from the target is calculated as:

$$N_{2n\text{-}air} = (N_{2n\text{-}calo} - N_{3n\text{-}air}W_{2+})/W_{2n}. \tag{8}$$

The number of detected $1n$ events $N_{1n\text{-}calo}$ equals to the sum of $1n$ events corrected for the neutron absorption in air, single neutrons from $2n$ events when one of the neutrons is lost and single neutrons from $3n$ events when two other neutrons interact with air:

$$N_{1n\text{-}calo} = N_{1n\text{-}air}W_{nN} + N_{2n\text{-}air}W_{1+} + N_{3n\text{-}air}W_{1++}. \tag{9}$$

Then the number of $1n$ events at the moment of neutron escape from the target is calculated as:

$$N_{1n\text{-}air} = (N_{1n\text{-}calo} - N_{2n\text{-}air}W_{1+} - N_{3n\text{-}air}W_{1++})/W_{nN}. \tag{10}$$

Table 4
Numbers of $1n$, $2n$ and $3n$ events $N_{*n\text{-}calo}$ $(* = 1, 2, 3)$ registered by the neutron calorimeter after the propagation of neutrons in air and the numbers of corresponding events $N_{*n\text{-}air}$ in the vicinity of the target.

Target	Channel	$N_{*n\text{-}calo}$	$N_{*n\text{-}air}$
Al	$1n$	916 500	918 247
	$2n$	382 800	386 307
	$3n$	157 074	162 894
Cu	$1n$	1 604 000	1 610 282
	$2n$	538 100	543 756
	$3n$	201 438	208 901
Sn	$1n$	634 000	636 720
	$2n$	203 000	205 181
	$3n$	74 738	77 507
Pb thin	$1n$	1 243 000	1 248 552
	$2n$	388 700	393 610
	$3n$	123 521	128 097
Pb thick	$1n$	1 330 000	1 337 861
	$2n$	461 600	466 786
	$3n$	163 885	169 957

The equations given in this section provide $N_{*n\text{-}air}$ defined as numbers of events characterized by specific $(* = 1, 2, 3)$ numbers of neutrons escaped from the target. The values of $N_{*n\text{-}air}$ are calculated from the corresponding counts $N_{*n\text{-}calo}$ of the neutron calorimeter. The resulting values are summarized in Table 4.

6.2. *Corrections for neutron loss in target material*

Once the probabilities of neutron interaction in target material are calculated, numbers of forward neutrons produced inside the target can be estimated by correcting the numbers of neutrons at their exit from the target, $N_{*n\text{-}air}$, obtained in Section 6.1. Similar to Eq. (2) written there, the mean free path λ_t of secondary neutrons before they interact with target nuclei is given as:

$$\lambda_t = A/(N_A \times \rho \times \sigma_{ntot}). \tag{11}$$

Here the density ρ for each target material is used, see Table 2. The total cross sections of neutron interaction with various target nuclei σ_{ntot} were also calculated by the Glauber theory [24]. They are listed in Table 5 together with measured cross sections [25]. Calculated σ_{ntot} well agrees with data for lead, but found by 15–20% lower than the data for other target nuclei.

In the following consideration it is assumed that EMD of indium nuclei is equally probable at any depth inside the target. This means that, the points of neutron emission are also evenly distributed along the beam path inside the target material. This assumption is valid when the attenuation of indium beam over the target depth d is relatively weak. The probability of neutron propagation without interaction until it reaches the depth x in the target is calculated as:

$$P(x) = \mathrm{e}^{-x/\lambda_t}. \tag{12}$$

Then the probability of neutron escape from the target without interaction is calculated as:

Table 5
Total cross section σ_{ntot} (millibarns) of interaction of high-energy neutrons with nuclei used in calculating neutron absorption in the target material. Measured cross sections from Refs. [26,29–31] are given for comparison.

Target	Theory	Experiment		
	σ_{ntot} (mb)	Cross section (mb)	Energy (GeV)	Experiment
Al	510	623 ± 12	149 ± 20	[29]
		634.8 ± 2.8	179 ± 26	[31]
Cu	970	1206 ± 19	149 ± 20	[30]
		1223 ± 6	179 ± 26	[31]
Sn	1530	1981 ± 7	54 ± 10	[26]
Pb	2960	3037 ± 47	149 ± 20	[30]
		2951 ± 28	179 ± 26	[31]

Table 6
The mean free path of neutrons, the probabilities of absorption for neutrons produced in $1n$, $2n$ and $3n$ events in various targets used in this experiment.

Target	λ_t (cm)	W_{nt}	W_{2nt}	W_{3nt}	W_{1+}	W_{2+}	W_{1++}
Al	32.560	0.971	0.943	0.916	0.057	0.061	0.0013
Cu	12.228	0.982	0.964	0.947	0.036	0.053	0.0001
Sn	17.668	0.990	0.981	0.970	0.019	0.028	0.0002
Pb thin	10.281	0.993	0.987	0.979	0.013	0.019	0.0001
Pb thick	10.281	0.986	0.972	0.959	0.028	0.041	0.0006

$$W_{nt} = \frac{1}{d}\int_0^d P(x)\,\mathrm{d}x = \frac{1}{d}\int_0^d \mathrm{e}^{-x/\lambda_t}\,\mathrm{d}x = \frac{\lambda_t}{d}\left(1 - \mathrm{e}^{-d/\lambda_t}\right). \tag{13}$$

Similar to the neutron absorption in air discussed in Section 6.1 the probability of escape of both produced neutrons from the target is $W_{2nt} = W_{nt}^2$, and $W_{3nt} = W_{nt}^3$ for all three produced neutrons. The probability of escape without interaction of only one from a pair of produced neutrons, with the other neutron absorbed in the target or deflected from the direction towards the calorimeter is estimated as:

$$W_{1+} = 2W_{nt}(1 - W_{nt}). \tag{14}$$

The probability of the event with two of three produced neutrons which leave the target without interaction, while the third one is absorbed or deflected, is calculated as:

$$W_{2+} = 3W_{nt}^2(1 - W_{nt}). \tag{15}$$

Finally, for the event with the escape of only one of the three produced neutrons the probability is given by:

$$W_{1++} = 3W_{nt}(1 - W_{nt})^2. \tag{16}$$

The above-defined probability values are summarized in Table 6 together with λ_t for each target used in our measurements.

The probabilities listed in Table 6 can be used now in calculating numbers of true $1n$, $2n$ and $3n$ events inside the target, $N_{1n\text{-}target}$, $N_{2n\text{-}target}$ and $N_{3n\text{-}target}$, from the numbers of events

$N_{1n\text{-}air}$, $N_{2n\text{-}air}$ and $N_{3n\text{-}air}$ at the exit from the target. Interactions of EMD neutrons inside the target lead to the loss of their energy and deflection from the forward direction. As a result, interacting neutrons are not registered by the neutron calorimeter as neutrons from EMD with their characteristic energy close to the beam energy per nucleon.

For $3n$ events:

$$N_{3n\text{-}air} = N_{3n\text{-}target} W_{3nt}, \tag{17}$$

and, respectively:

$$N_{3n\text{-}target} = N_{3n\text{-}air} / W_{3nt}. \tag{18}$$

The events with two forward neutrons leaving the target include true $2n$ events corrected for neutron absorption and also $3n$ events with one neutron lost in interactions with target material:

$$N_{2n\text{-}air} = N_{2n\text{-}target} W_{2nt} + N_{3n\text{-}target} W_{2+}, \tag{19}$$

and, respectively:

$$N_{2n\text{-}target} = (N_{2n\text{-}air} - N_{3n\text{-}target} W_{2+}) / W_{2nt}. \tag{20}$$

The number of $1n$ events at the exit from the target surface consists of true $1n$ events with its number corrected for absorption. In addition, it includes single neutrons from those $2n$ and $3n$ events, where one or two neutrons, respectively, were absorbed or scattered in the target:

$$N_{1n\text{-}air} = N_{1n\text{-}target} W_{nt} + N_{2n\text{-}target} W_{1+} + N_{3n\text{-}target} W_{1++}. \tag{21}$$

This gives:

$$N_{1n\text{-}target} = (N_{1n\text{-}air} - N_{2n\text{-}target} W_{1+} - N_{3n\text{-}target} W_{1++}) / W_{nt}. \tag{22}$$

The values of $N_{1n\text{-}air}$, $N_{2n\text{-}air}$, $N_{3n\text{-}air}$ and $N_{1n\text{-}target}$, $N_{2n\text{-}target}$, $N_{3n\text{-}target}$ for each target are listed in Table 7.

6.3. Corrections for multiple EMD events

Following EMD of a beam nucleus leading to the emission of few neutrons from ^{115}In, a further EMD process of a residual nucleus can also take place. Therefore, two subsequent EMD events can take place in the target after the entry of a single beam nucleus, and appropriate corrections to $N_{*n\text{-}target}$ are necessary. One can assume that the total EMD cross section for the nuclear residue in the second EMD process is approximately equal to the corresponding cross section for primary ^{115}In nuclei. Due to a relatively small target thickness the third EMD process can be neglected.

The mean free path of ^{115}In in target material with respect to the EMD process with emission of a single neutron, λ_{1n}, is calculated as:

$$\lambda_{1n} = A / (N_A \times \rho \times \sigma_{1n}), \tag{23}$$

where σ_{1n} is the cross section of $1n$-emission as a result of EMD, which is calculated by the RELDIS model, see Table 1, and ρ is the density of target material, see Table 2. One can also assume that the probabilities of single and double EMD obey a Poisson distribution characterized by the average number of $1n$ events:

Table 7
Numbers of events $N_{*n\text{-}air}$ with given number of neutrons ($* = 1, 2, 3$) which leave the target in the direction of the neutron calorimeter and true numbers $N_{*n\text{-}target}$ of events inside the target for each neutron multiplicity.

Target	Channel	$N_{*n\text{-}air}$	$N_{*n\text{-}target}$
Al	$1n$	918 247	921 255
	$2n$	386 307	392 140
	$3n$	162 894	173 640
Cu	$1n$	1 610 282	1 619 825
	$2n$	543 756	552 057
	$3n$	208 901	220 744
Sn	$1n$	636 720	638 890
	$2n$	205 181	206 875
	$3n$	77 507	79 775
Pb thin	$1n$	1 248 552	1 251 570
	$2n$	393 610	396 245
	$3n$	128 097	130 643
Pb thick	$1n$	1 337 861	1 343 585
	$2n$	466 786	472 758
	$3n$	169 957	177 388

$$\mu = 1 - \mathrm{e}^{-d/\lambda_{1n}}, \tag{24}$$

where d is the target thickness. Therefore, the probability of the event when a beam nucleus propagates through the target without interaction is calculated as:

$$P_0 = \mathrm{e}^{-\mu}, \tag{25}$$

while the probability of a single $1n$ EMD event is:

$$P_1 = \mu \mathrm{e}^{-\mu}. \tag{26}$$

The probability of two subsequent $1n$ EMD events is:

$$P_2 = \frac{\mu^2}{2}\mathrm{e}^{-\mu}. \tag{27}$$

Following these relations the ratio between double and single EMD events with $1n$ emission equals to $P_2/P_1 = \mu/2$. Since a pair of two subsequent $1n$ emissions inside the target is identified by the calorimeter as a single $2n$ event, the number of true $1n$ events N_{1n} is calculated by introducing a correction to $N_{1n\text{-}target}$:

$$N_{1n} = N_{1n\text{-}target}(1 + 2P_2/P_1). \tag{28}$$

Finally, the number of true $2n$ events N_{2n} is calculated by subtracting the number of double $1n$ events:

$$N_{2n} = N_{2n\text{-}target} - N_{1n\text{-}target}P_2/P_1. \tag{29}$$

The results for N_{1n} and N_{2n} obtained after this correction are summarized in Table 8.

Table 8
Mean free path λ_{1n} of 158A GeV ^{115}In in target material with respect to $1n$ emission in EMD, the average number μ of such events for a given target, and the numbers, N_{1n} and N_{2n}, of true $1n$ and $2n$ events after correction for multiple $1n$ events.

Target	Channel	λ_{1n} (cm)	μ	N_{*n}
Al	$1n$	41.828	0.0329	982 910
	$2n$			361 312
Cu	$1n$	6.217	0.0698	1 854 084
	$2n$			434 927
Sn	$1n$	4.94	0.0665	726 747
	$2n$			162 947
Pb thin	$1n$	2.166	0.0604	1 407 463
	$2n$			318 299
Pb thick	$1n$	2.166	0.1267	1 707 008
	$2n$			291 046

Table 9
The mean free path of ^{115}In nuclei in the target materials with respect to hadronic fragmentation and the corresponding attenuation factor.

Target	λ_{nuc} (cm)	P_{nuc}
Al	4.97	0.755
Cu	2.79	0.851
Sn	5.26	0.937
Pb thin	4.92	0.973
Pb thick	4.92	0.942

6.4. *Corrections for hadronic fragmentation of ^{115}In in the target*

Beam nuclei propagating through the target initiate electromagnetic as well as hadronic collisions with target nuclei. A part of beam nuclei is destroyed in hadronic interactions. Therefore, the beam of ^{115}In nuclei is attenuated due to hadronic nucleus–nucleus collisions, and the corresponding correction factor P_{nuc} have to be applied to N_{*n}:

$$P_{nuc} = \mathrm{e}^{-d/\lambda_{nuc}}, \tag{30}$$

where $\lambda_{nuc} = 1/n\sigma_{nuc}$ with n defined as the density of nuclei in the target material and σ_{nuc} as the total hadronic cross section listed in Table 1.

The correction factors are listed in Table 9 for each target. They are especially important for Al and Cu targets.

7. Final results and discussion

The final results of our study for the cross sections of $1n$, $2n$ and $3n$ emission in EMD along with the correction factors applied at each step of the analysis are presented in Table 10. As seen, the corrections are essential for $1n$ cross sections measured for all targets. Due to relatively large σ_{nuc} compared to the EMD cross sections, the corrections introduced for Al target are important

Table 10
Uncorrected $1n$, $2n$ and $3n$ emission EMD cross sections for 158A GeV ^{115}In on Al, Cu, Sn and Pb, correction factors for neutron absorption in air, in the target, for double EMD and for hadronic processes which are progressively applied in each column. Resulting cross sections are given in the last column.

Target	EMD channel	Uncorrected cross section (barns)	Air	Air + target	Air + target + double EMD	Air + target + double EMD + hadronic	Cross section (barns)
Al	$1n$	0.395	1.00191	1.00519	1.072462	1.421263	0.562
	$2n$	0.167	1.00916	1.02440	0.943868	1.250846	0.209
	$3n$	0.0667	1.00191	1.00519	–	1.332111	0.0888
Cu	$1n$	1.541	1.00392	1.00987	1.155918	1.358164	2.093
	$2n$	0.515	1.01051	1.02594	0.808267	0.949686	0.489
	$3n$	0.189	1.00392	1.00987	–	1.186563	0.224
Sn	$1n$	4.090	1.00429	1.00771	1.146285	1.222837	5.001
	$2n$	1.300	1.01074	1.01909	0.802694	0.856300	1.113
	$3n$	0.471	1.00429	1.00771	–	1.075008	0.507
Pb thin	$1n$	9.779	1.00447	1.00689	1.132306	1.163778	11.381
	$2n$	3.050	1.01263	1.01941	0.818879	0.841640	2.567
	$3n$	0.953	1.00447	1.00689	–	1.034876	0.986
Pb thick	$1n$	9.750	1.00365	1.00794	1.2805753	1.359360	13.254
	$2n$	3.327	1.01124	1.02417	0.630515	0.669306	2.227
	$3n$	1.150	1.00365	1.00794	–	1.069952	1.230

for all EMD channels. At the same time the corrections for $3n$ cross sections on Sn and Pb targets are small.

The measured cross sections are compared to ones calculated with RELDIS in Table 11. Calculated cross sections itself typically have uncertainties at the level of 5–7% due to uncertainties in photonuclear cross sections used as input in calculations.

Due to a large number ($> 10^4$) of events registered by the calorimeter for each neutron multiplicity the statistical uncertainties of our measurements are small, below 0.3%, and can be neglected. Therefore, only systematical uncertainties are listed in Table 11. They are attributed mostly to uncertainties in corrections applied to account for the absorption of beam nuclei and produced neutrons. Such corrections introduced to data obtained with both thin and thick Pb targets should give same results in principle. Once the cross sections estimated from measurements with this pair of targets diverge, this difference can be considered as a systematical uncertainty of our analysis. As follows from Table 11, this difference is $\sim 15\%$ for $1n$ and $2n$ channels and $\sim 20\%$ for $3n$ channel. The same relative uncertainties were attributed to the cross sections measured with other three targets.

As seen from Table 11, the measured cross sections of forward neutron emission in collisions of ^{115}In with Cu, Sn and Pb agree well with RELDIS taking into account the uncertainties of measurements listed in the table. However, the data for Al for all neutron multiplicities are noticeably larger compared to RELDIS results for this target nucleus.

A convenient presentation of the data and calculations is given in Fig. 9, where all cross sections are divided by Z^2, the square of charge of target nuclei, and plotted as a function of Z. As expected, the spectrum of equivalent photons is approximately proportional to Z^2 of the target nuclei (Al, Cu, Sn, or Pb), which emit photons absorbed by ^{115}In. This is illustrated by a flat dependence of RELDIS results divided by Z^2 as a function of Z with its slight increase

Table 11
Measured $1n$, $2n$ and $3n$ emission EMD cross sections for 158A GeV ^{115}In on Al, Cu, Sn and Pb and cross sections calculated with RELDIS. Experimental errors are only due to systematical uncertainties of corrections introduced for the absorption of beam nuclei and produced neutrons in the target material and air.

Target	EMD channel	Experiment (barns)	RELDIS (barns)
Al	$1n$	0.56 ± 0.08	0.40
	$2n$	0.21 ± 0.03	0.09
	$3n$	0.09 ± 0.02	0.03
Cu	$1n$	2.09 ± 0.31	1.91
	$2n$	0.49 ± 0.07	0.45
	$3n$	0.22 ± 0.04	0.13
Sn	$1n$	5.00 ± 0.75	5.47
	$2n$	1.11 ± 0.17	1.28
	$3n$	0.5 ± 0.1	0.38
Pb thin	$1n$	11.4 ± 1.7	14.05
	$2n$	2.57 ± 0.38	3.32
	$3n$	0.99 ± 0.20	1.03
Pb thick	$1n$	13.25 ± 2.00	14.05
	$2n$	2.23 ± 0.33	3.32
	$3n$	1.23 ± 0.25	1.03

for lighter targets. This increase is explained by a wider range of impact parameters available in ultraperipheral collisions with light targets defined by $b > R_1 + R_2$, see Section 2. This provides higher E_{max} for Al and Cu compared to Pb target. Despite of this peculiarity a flat dependence of σ/Z^2 serves as a clear indication of the electromagnetic nature of interactions. In particular, a similar flat dependence was observed in our studies of the emission of forward neutrons by 30A GeV Pb nuclei in collisions with Al, Cu, Sn and Pb [14].

Taking into account experimental uncertainties of the present data, σ/Z^2 for Cu, Sn and Pb targets are consistent in general with a flat dependence on Z. However, the cross sections measured with Al target are higher than calculated with RELDIS, and also a general descending trend of σ/Z^2 is obvious in Fig. 9. As follows from Table 1, the cross sections of $1n$, $2n$ and $3n$ emission in hadronic interactions of ^{115}In with Al are comparable to the corresponding EMD cross sections. Therefore, a noticeable contribution of hadronic events to the emission of forward neutrons by ^{115}In in collisions with Al is expected. Apart of the EMD process, one, two and three neutrons are also produced in peripheral grazing hadronic nucleus–nucleus collisions. For a given projectile nucleus the cross section of grazing collisions is proportional to the area of a thin surface rim of the target nucleus: $\sigma \sim Z^{2/3}$. This means that $\sigma/Z^2 \sim 1/Z^{4/3}$, and the descending trend which is seen in Fig. 9 due the presence of hadronic events is thus explained.

8. Conclusions

The cross sections of emission of one, two and three forward neutrons in collisions of 158A GeV ^{115}In projectiles with Al, Cu, Sn and Pb target nuclei are measured. The collected data are compared with the cross sections of neutron emission in electromagnetic dissociation of ^{115}In calculated with the RELDIS model. The measured cross sections agree with the cross sections

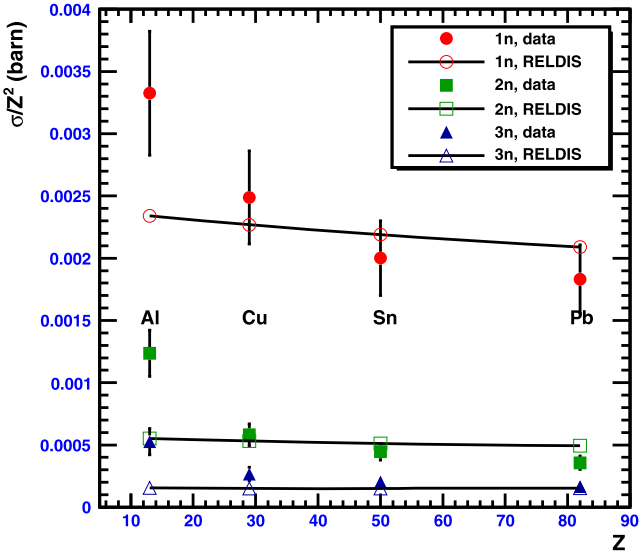

Fig. 9. Cross sections of emission of one, two and three neutrons by 158A GeV ^{115}In as a function of the target nuclei charge Z. Measured $1n$, $2n$ and $3n$ cross sections are shown by circles, squares and triangles, respectively. Open symbols connected by a solid line represent RELDIS results. All values are divided by Z^2 to demonstrate the characteristic dependence of the EMD cross sections.

calculated by RELDIS for ultraperipheral collisions with Cu, Sn and Pb targets within estimated uncertainties of the measurements. Such systematic uncertainties stem from the corrections to raw data accounting for interactions of projectile nuclei and neutrons with target material and air. The validity of the RELDIS model for simulating electromagnetic dissociation of ultrarelativistic ^{115}In nuclei is demonstrated.

The measured cross sections are attributed mainly to the electromagnetic dissociation process, as their values divided by Z^2 of the target nucleus demonstrate a weak dependence on Z. The excess of neutron emission cross section measured in In–Al collisions with respect to calculated EMD cross section indicates a noticeable contribution of grazing In–Al collisions. This is in contrast to our previous experiment [14] conducted with 30A GeV ^{208}Pb beam colliding with the same targets where the contribution of grazing collisions was found relatively small with respect to EMD also for Al target.

As demonstrated recently [4,5], ultraperipheral collisions of lead nuclei followed by emission of forward neutrons play a certain role at the LHC collider due to their large cross sections. Forward neutron emission can be used to monitor the LHC luminosity, providing that such cross sections are known with sufficient accuracy, e.g., calculated with RELDIS.

As shown [4,5], such cross sections are indeed reliably predicted by RELDIS, once this model has been previously validated by comparison with the data [14] also collected with ultrarelativistic Pb projectiles, but at lower energies.

Our present results confirm the accuracy of RELDIS in describing the cross sections of forward neutron emission by medium-weight ultrarelativistic ^{115}In nuclei. Therefore, the RELDIS model can be also used to plan future experiments at the LHC, possibly with beams of medium-weigh nuclei, like ^{115}In. New experiments on photoabsorption on various target nuclei are very desirable, as they help to improve the accuracy of nuclear data used to model EMD.

Acknowledgements

This work was supported by the Russian Foundation for Basic Research, grant No. 12-02-91508-CERN and by the Program of the Russian Academy of Sciences RAS-CERN. The authors are very grateful to V.V. Varlamov for discussions of photonuclear data on ^{115}In.

References

[1] C.A. Bertulani, G. Baur, Phys. Rep. 163 (1988) 299.
[2] G. Baur, K. Hencken, D. Trautmann, S. Sadovsky, et al., Phys. Rep. 364 (2002) 359.
[3] A.J. Baltz, G. Baur, D. d'Enterria, et al., Phys. Rep. 458 (2008) 1.
[4] C. Oppedisano, J. Phys. G 38 (2011) 124174.
[5] B. Abelev, et al., ALICE Collaboration, Phys. Rev. Lett. 109 (2012) 252302.
[6] A.J. Baltz, M.J. Rhoades-Brown, J. Weneser, Phys. Rev. C 54 (1996) 4233.
[7] S.R. Klein, Nucl. Instrum. Methods A 459 (2001) 51.
[8] R. Bruce, D. Bocian, S. Gilardoni, et al., Phys. Rev. ST Accel. Beams 12 (2009) 071002.
[9] A.J. Baltz, C. Chasman, S.N. White, Nucl. Instrum. Methods A 417 (1998) 1.
[10] I.A. Pshenichnov, J.P. Bondorf, I.N. Mishustin, et al., Phys. Rev. C 64 (2001) 024903.
[11] I.A. Pshenichnov, Phys. Part. Nucl. 42 (2011) 215.
[12] I.A. Pshenichnov, I.N. Mishustin, J.P. Bondorf, et al., Phys. Rev. C 57 (1998) 1920.
[13] I.A. Pshenichnov, I.N. Mishustin, J.P. Bondorf, et al., Phys. Rev. C 60 (1999) 044901.
[14] M.B. Golubeva, F.F. Guber, T.L. Karavicheva, et al., Phys. Rev. C 71 (2005) 024905.
[15] U.I. Uggerhøj, I.A. Pshenichnov, C. Scheidenberger, et al., Phys. Rev. C 72 (2005) 057901.
[16] J.P. Bondorf, A.S. Botvina, A.S. Iljinov, I.N. Mishustin, K. Sneppen, Phys. Rep. 257 (1995) 133.
[17] O.V. Bogdankevich, B.I. Goryachev, V.A. Zapevalov, J. Exp. Theor. Phys. 15 (1962) 1044.
[18] S.C. Fultz, B.L. Berman, J.T. Caldwell, R.L. Bramblett, M.A. Kelly, Phys. Rev. 186 (1969) 1255.
[19] A. Leprêtre, H. Beil, R. Bergère, P. Carlos, A. De Miniac, A. Veyssière, K. Kernbach, Nucl. Phys. A 219 (1974) 39.
[20] V.V. Varlamov, B.S. Ishkhanov, V.N. Orlin, A.V. Sopov, Preprint SINP MSU 2010-8/864 (in Russian).
[21] Experimental Nuclear Reaction Data (EXFOR), http://www-nds.iaea.org/exfor/exfor.htm.
[22] B.L. Berman, B.L. Fultz, Rev. Mod. Phys. 47 (1975) 713.
[23] S.S. Dietrich, B.L. Berman, At. Data Nucl. Data Tables 38 (1988) 199.
[24] C. Scheidenberger, I.A. Pshenichnov, K. Sümmerer, et al., Phys. Rev. C 70 (2004) 014902.
[25] V.S. Barashenkov, Cross Sections of Interactions of Particles and Nuclei with Nuclei, JINR, Dubna, 1993.
[26] A.I. Babaev, E.V. Brehman, Yu.V. Galaktionov, et al., Yad. Fis. 20 (1974) 71 (in Russian).
[27] H. Palevsky, J.L. Frides, R.J. Sutter, et al., Phys. Rev. Lett. 18 (1967) 1200.
[28] Kh.P. Babayan, N.L. Grigorov, E.Ya. Mamizhdanyan, et al., Izv. Acad. Nauk SSSR, Ser. Fis. 29 (1965) 1652 (in Russian).
[29] J. Biel, E. Bleser, C. Bromberg, et al., Phys. Rev. Lett. 36 (1976) 1004.
[30] G.K. Bisheva, V.S. Borisov, L.L. Goldin, et al., Phys. Lett. B 24 (1967) 533.
[31] V.R. Murthy, C.A. Ayre, H.R. Gustafson, et al., Nucl. Phys. B 92 (1975) 269.